

# Tailored $\text{Cl}^-$ Ligation on Supported Pt Catalysts for Selective Primary C–H Bond Oxidation

Chunyan Ma, Chenggong Yang, Hongying Zhuo, Cheng Chen, Ke Lu, Fengbang Wang, Zhifu Shi, Hai Xiao,\* Maoyong Song,\* and Guibin Jiang



Cite This: *J. Am. Chem. Soc.* 2023, 145, 10890–10898



Read Online

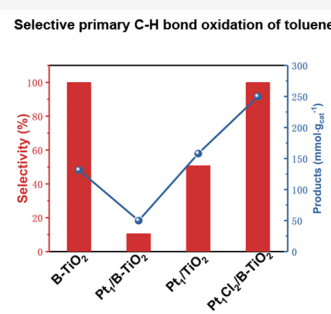
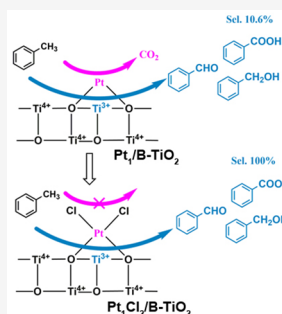
ACCESS |

Metrics & More

Article Recommendations

Supporting Information

**ABSTRACT:** It is challenging to achieve high selectivity over Pt-metal-oxide catalysts widely used in many selective oxidation reactions because Pt is prone to over-oxidize substrates. Herein, our sound strategy for enhancing the selectivity is to saturate the under-coordinated single Pt atoms with  $\text{Cl}^-$  ligands. In this system, the weak electronic metal–support interactions between Pt atoms and reduced  $\text{TiO}_2$  cause electron extraction from Pt to  $\text{Cl}^-$  ligands, resulting in strong Pt–Cl bonds. Therefore, the two-coordinate single Pt atoms adopt a four-coordinate configuration and thus inactivated, thereby inhibiting the over-oxidation of toluene over Pt sites. The selectivity for the primary C–H bond oxidation products of toluene was increased from 50.1 to 100%. Meanwhile, the abundant active  $\text{Ti}^{3+}$  sites were stabilized in reduced  $\text{TiO}_2$  by Pt atoms, leading to a rising yield of the primary C–H oxidation products of 249.8  $\text{mmol g}_{\text{cat}}^{-1}$ . The reported strategy holds great promise for selective oxidation with enhanced selectivity.



Downloaded via TSINGHUA UNIV on July 31, 2023 at 06:20:09 (UTC).  
See https://pubs.acs.org/sharingguidelines for options on how to legitimately share published articles.

## INTRODUCTION

Oxide-supported Pt catalysts have been used in many important chemical reactions. In particular, high-performance supported Pt catalysts have been designed for the production of fine chemicals via selective oxidation,<sup>1–4</sup> dehydrogenation,<sup>5,6</sup> and hydrogenation.<sup>7,8</sup> However, byproducts are produced because of over-oxidation,<sup>1–4</sup> deep dehydrogenation,<sup>5,6</sup> or unselective hydrogenation.<sup>7,8</sup> Generally, selectivity can be enhanced by tailoring the metal–support interfaces,<sup>9,10</sup> engineering the local geometry and electronic environment around the Pt sites,<sup>11,12</sup> or tuning the coordination structure of the oxide supports.<sup>13</sup> Unfortunately, the increase in selectivity is limited by the high activity of the Pt sites.<sup>9–13</sup> Another strategy is to modify supported Pt catalysts with organic inhibitors, such as nitrogen-containing organics (e.g., alkyl amines)<sup>14,15</sup> or sulfur-containing organics (e.g., mercaptan).<sup>16</sup> However, organic inhibitors always reduce the catalytic activity because of their coverage of the catalyst surface. Therefore, a strategy for enhancing selectivity without sacrificing catalytic activity is urgently required.

Electron donor–acceptor interactions between platinum and metal oxides, in which platinum donates electrons to metal oxides, result in the formation of interfacial metal sites with low-oxidation states in the oxide support. These low-oxidation-state metal sites are electron-rich and can interact with adsorbate molecules and activate them in certain reaction processes.<sup>17–19</sup> For example,  $\text{Ti}^{3+}$  sites confined to platinum atoms act as active sites for selective glycerol oxidation,<sup>17</sup> the

water–gas shift reaction,<sup>18</sup> and  $\text{C}=\text{O}$  bond hydrogenation.<sup>19</sup> In our previous study, we demonstrated that the fabrication of stable  $\text{Ti}^{3+}$  sites using nitrogen-doped  $\text{TiO}_2$  improves the catalytic activity for solvent-free selective oxidation of toluene, thus enhancing the yield of primary C–H bond oxidation products, including benzyl alcohol, benzaldehyde, benzoic acid, and benzyl benzoate.<sup>20</sup> Toluene oxidation to produce primary C–H bond oxidation products is an attractive but significantly challenging transformation. A variety of metal-based catalysts have been developed, such as vanadium,<sup>21,22</sup> manganese,<sup>23</sup> copper,<sup>24,25</sup> or cobalt<sup>26,27</sup> catalysts (Table S1). However, the use of peroxide as an oxidant for these transformations in an organic solvent is environmentally unfriendly. A solvent-free system with oxygen as the oxidant is still challenging because of low conversion and poor yield (Table S2). Pd-PMHS/ $\text{TiO}_2$  achieves 100% selectivity for primary C–H bond oxidation products, but the yield of the primary C–H bond oxidation product is 15.9  $\text{mmol g}_{\text{cat}}^{-1}$ .<sup>28</sup> AuPd/ $\text{TiO}_2$  achieves benzyl benzoate with 95.5% selectivity, but it also achieved a low primary C–H bond oxidation product yield of 59.5  $\text{mmol g}_{\text{cat}}^{-1}$ .<sup>29</sup>

Received: March 29, 2023

Published: May 8, 2023



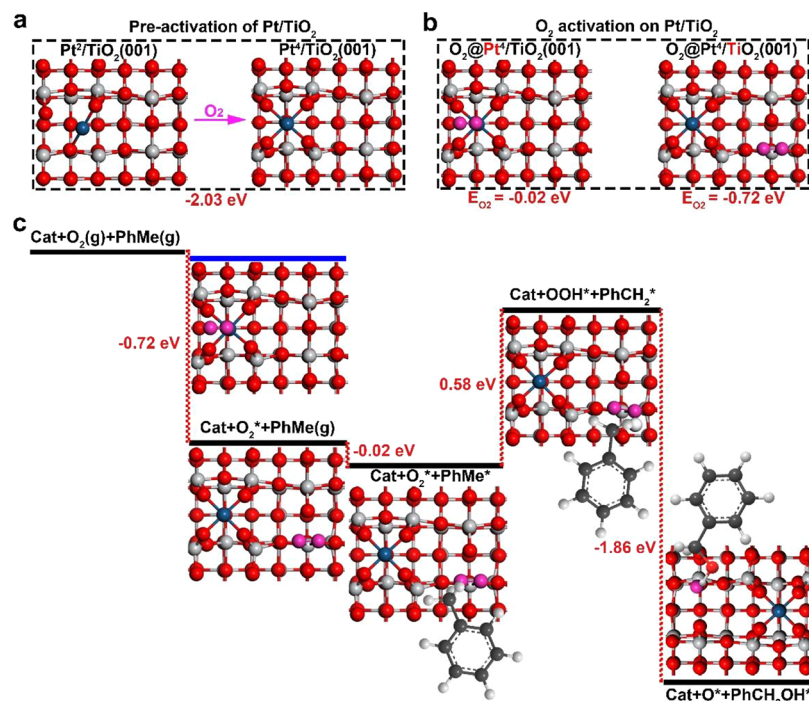


**Figure 1.** DFT calculations of selective oxidation of toluene over Pt/TiO<sub>2</sub>. **a**, DFT calculation results for the pre-activation of Pt/TiO<sub>2</sub>. **b**, O<sub>2</sub> activation energy at four-coordinate Pt<sub>1</sub> and Ti sites. **c**, Energy profiles for the C–H activation process on Pt<sub>1</sub>/TiO<sub>2</sub>. The black line represents the energy profile at the Ti site, whereas the blue line represents the profile at the four-coordinate Pt<sub>1</sub> site. Pt, Ti, O, adsorbed O, C, and H are shown in blue, light gray, red, magenta, dark gray, and white, respectively.

The use of TiO<sub>2</sub>-supported platinum results in the formation of interfacial Ti<sup>3+</sup> sites via efficient electron transfer from Pt to TiO<sub>2</sub>,<sup>30</sup> which provides potential to enhance the activity of selective oxidation of toluene further. However, in this process, oxygen activated over Pt sites greatly facilitates the over-oxidation of C–H bonds to CO<sub>2</sub>. Then, a key issue facing Pt/TiO<sub>2</sub> catalysts is the need to inhibit over-oxidation and achieve high selectivity. An aqueous solution of chloroplatinic acid (H<sub>2</sub>PtCl<sub>6</sub>·H<sub>2</sub>O) is the most commonly used precursor for the synthesis of Pt/TiO<sub>2</sub>, but the Cl<sup>−</sup> ligands are usually removed by washing with ultrapure water, followed by calcination, because the Pt–Cl bonds could lead to the sintering of Pt atoms during the reaction<sup>31–33</sup> and also have a negative effect on heterogeneous catalytic activity.<sup>34,35</sup> However, in this study, by means of density functional theory (DFT), we reveal that two-coordinate single Pt sites are highly active for O<sub>2</sub>, but four-coordinate single Pt sites can barely adsorb O<sub>2</sub>. Thus, we aimed to maintain the Cl<sup>−</sup> ligands and Pt–Cl bonds to obtain Pt-saturated coordination and thus deactivated single Pt sites. Using this approach, we can avoid the over-oxidation of toluene on single Pt sites. Therefore, in this study, Pt single atoms were supported on reduced TiO<sub>2</sub> (denoted B-TiO<sub>2</sub>) catalysts. First, many Ti<sup>3+</sup> sites in B-TiO<sub>2</sub> were stabilized with electron-rich Pt atoms to increase the activity for the primary C–H bond oxidation of toluene. Furthermore, stable Pt–Cl bonds, which are difficult to break via washing and calcination, were formed. As a result, the selectivity for the primary C–H bond oxidation products of toluene was close to 100%, and the yield of the primary C–H bond oxidation product reached 249.8 mmol g<sub>cat</sub><sup>−1</sup>, which is 1.9 times as high as that obtained over B-TiO<sub>2</sub> and 4.2 times as high as that obtained over the reported AuPd/TiO<sub>2</sub> catalysts.<sup>29</sup> Our investigation of these B-TiO<sub>2</sub>-supported Pt single-atom catalysts full of Ti<sup>3+</sup> sites shows

that Pt–Cl bonds have a positive effect on the catalytic performance because of the deactivation of the Pt sites.

## RESULTS AND DISCUSSION

**Theoretical Investigation of the Deactivate Process of Single Pt Atoms.** To identify the active sites for the selective oxidation of toluene, DFT calculations were carried out with the starting model of one Pt single atom (Pt<sub>1</sub>) anchored on the anatase TiO<sub>2</sub>(001) surface. As shown in Figure S1, different anchoring sites for Pt<sub>1</sub> were considered and the results showed that the Pt<sub>1</sub> prefers the bridging site by connecting to one O<sub>2c</sub> and one O<sub>3c</sub>, with the Pt–O distances of 1.97 and 2.06 Å, respectively. Upon the initial O<sub>2</sub> activation, we found that the two-coordinate Pt<sub>1</sub> adopts a four-coordinate configuration with the lowest energy, as shown in Figure 1a. This implies that the high performance of the two-coordinate Pt<sub>1</sub> site for O<sub>2</sub> activation and the catalyst surface may go through a pre-activation process. Next, both the four-coordinate Pt<sub>1</sub> site and the interfacial Ti site were considered for further O<sub>2</sub> activation (Figures 1b and S2). We found that O<sub>2</sub> can barely adsorb on the four-coordinate Pt<sub>1</sub> site, while the Ti site can adsorb and activate O<sub>2</sub> easily with an adsorption energy of −0.72 eV. This indicates that the four-coordinate Pt<sub>1</sub> site is inactive for further primary C–H oxidation. Thus, we calculated the energy profile for the C–H bond hydroxylation of toluene by the Ti site via the rebound mechanism (Figure 1c).<sup>36</sup> The results show that this reaction requires only 0.58 eV to reach the key radical intermediate, with an energy release of 2.01 eV afterward, indicating that the Ti site is highly active for the primary C–H bond activation.

In addition, we also considered the dual-site mechanism, where C–H bonds are probably activated by the single noble metal atoms<sup>37</sup> and O<sub>2</sub> is activated by the interfacial Ti site. As

## Scheme

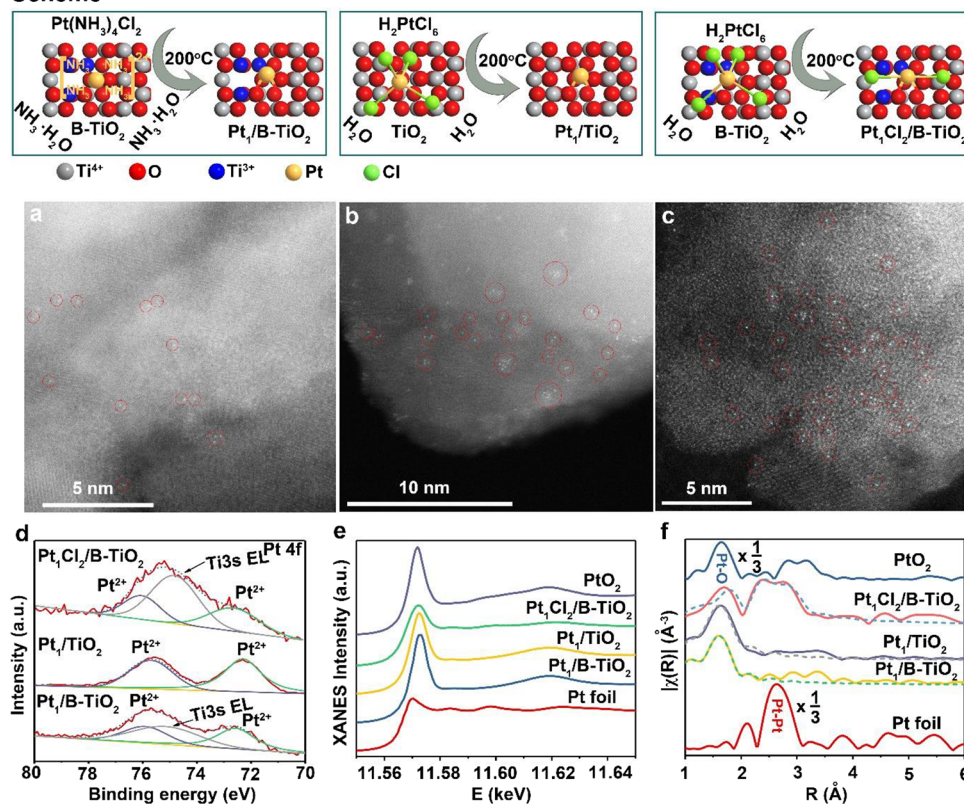


**Figure 2.** Synthetic scheme, Pt dispersion, and Pt valence of the Pt/TiO<sub>2</sub> catalysts. Scheme shows a schematic of loading Pt single atoms on TiO<sub>2</sub> or B-TiO<sub>2</sub>. a–c, ac-HAADF/STEM images of Pt<sub>1</sub>/B-TiO<sub>2</sub> (a), Pt<sub>1</sub>/TiO<sub>2</sub> (b), and Pt<sub>1</sub>Cl<sub>2</sub>/B-TiO<sub>2</sub> (c). d, Pt 4f XPS spectra of Pt/TiO<sub>2</sub> catalysts. e, Normalized XANES spectra at the Pt L<sub>3</sub> edge of Pt foil, PtO<sub>2</sub>, and Pt/TiO<sub>2</sub> catalysts. f, R-space of Pt K-edge of experimental (solid line) and calculated (dotted line) data of the K<sup>3</sup>-weighted Fourier transform spectra from EXAFS.

shown in Figure S3, the oxidation of the C–H bond by the four-coordinate Pt<sub>1</sub> site is a continuous energy increase process, especially the PhCH<sub>2</sub>OH desorption process, with an energy increase of 1.02 eV. The high energy increase was due to the break of the Pt–O bond where the O in Pt<sub>1</sub>O<sub>4</sub> moieties can be regarded as lattice O to some extent. The leaving three-coordinated Pt<sub>1</sub> then saturated by the pre-adsorbed O<sub>2</sub> at the Ti site, forming the stable four-coordinated Pt<sub>1</sub> site again with an energy release of 3.02 eV (Figure S4). Thus, it is reasonable to conclude that the four-coordinate Pt<sub>1</sub> site is inactive for C–H activation.

**Synthesis of Pt<sub>1</sub>Cl<sub>2</sub> on B-TiO<sub>2</sub>.** According to the DFT calculations, the two-coordinate Pt<sub>1</sub> site is the preferred configuration for TiO<sub>2</sub>. Fabricating a four-coordinated Pt<sub>1</sub> site directly avoids oxygen activation over the two-coordinate Pt<sub>1</sub> site. Here, the two-coordinate Pt<sub>1</sub> site could be coordinated with Cl<sup>−</sup> ligands to form a tetrahedral coordination geometry. The synthesis of the TiO<sub>2</sub>-supported Pt<sub>1</sub> site coordinated to Cl<sup>−</sup> ligands is shown in Figure 2 Scheme. First, a B-TiO<sub>2</sub>-supported Pt single atom catalyst (Pt<sub>1</sub>/B-TiO<sub>2</sub>) was synthesized using electrostatic adsorption. Electrostatic adsorption was carried out using tetraammineplatinum(II) chloride (TAPC, PtCl<sub>2</sub> 4(NH<sub>3</sub>)·H<sub>2</sub>O) as the precursor, and B-TiO<sub>2</sub> was dissolved in ammonium hydroxide. Ammonium hydroxide helps to wash off the Cl<sup>−</sup> ligands.<sup>38</sup> Furthermore, atomically dispersed Pt on TiO<sub>2</sub> and B-TiO<sub>2</sub> was synthesized using the impregnation method. This impregnation process was carried out using H<sub>2</sub>PtCl<sub>6</sub>·H<sub>2</sub>O as the precursor. At the Pt/TiO<sub>2</sub> interface, the electrons tend to transfer from the Pt single

atoms to the TiO<sub>2</sub> support, so fewer electrons are shared between the Pt atoms and Cl atoms. Thus, when using TiO<sub>2</sub> as a support, the Cl<sup>−</sup> ligands on Pt were easily removed by washing and calcination.<sup>39</sup> In contrast, at the Pt/B-TiO<sub>2</sub> interface, electron extraction from Pt is prone to transfer to the Cl<sup>−</sup> ligands adsorbed on Pt but not the electron-enriched B-TiO<sub>2</sub>. The strong electronic interaction between the Pt atoms and Cl<sup>−</sup> ligands makes the removal of Cl<sup>−</sup> ligands difficult, which results in strong Pt–Cl bonds. The TiO<sub>2</sub>-supported Pt single-atom catalyst prepared using the impregnation method is denoted Pt<sub>1</sub>/TiO<sub>2</sub>, and the B-TiO<sub>2</sub>-supported Pt single-atom catalyst prepared using the impregnation method is denoted Pt<sub>1</sub>Cl<sub>2</sub>/B-TiO<sub>2</sub>.

Figure 2a–c shows aberration-corrected high-angle annular dark-field scanning transmission electron microscopy (ac-HAADF/STEM) images of Pt<sub>1</sub>/B-TiO<sub>2</sub>, Pt<sub>1</sub>/TiO<sub>2</sub>, and Pt<sub>1</sub>Cl<sub>2</sub>/B-TiO<sub>2</sub>, respectively. Contact points consistent with the imaging of single platinum atoms were observed, as shown by the red circles. It is noted that single Pt atoms locate beside the Ti atoms but not by replacing Ti atoms in Pt<sub>1</sub>/TiO<sub>2</sub>, which indicates that Pt<sub>1</sub> adsorbed on TiO<sub>2</sub> and coordinated by O atoms in the DFT model (Figures 1 and S1) was reasonable. In the number of STEM images of Pt<sub>1</sub>Cl<sub>2</sub>/B-TiO<sub>2</sub>, it has been found that there was a Pt nanoparticle with a diameter of ~1 nm among Pt single-atom distribution (Figure S5).

X-ray diffraction (XRD) patterns of TiO<sub>2</sub>, B-TiO<sub>2</sub>, Pt<sub>1</sub>/B-TiO<sub>2</sub>, Pt<sub>1</sub>/TiO<sub>2</sub>, and Pt<sub>1</sub>Cl<sub>2</sub>/B-TiO<sub>2</sub> revealed that the crystalline planes were well maintained, even after reduction treatment or the addition of Pt (Figure S6). Furthermore, the

Table 1. EXAFS Fitting Parameters at the Pt L<sub>3</sub>-Edge for Pt/TiO<sub>2</sub> Samples

sample	shell	<i>N</i> <sup>a</sup>	<i>R</i> (Å) <sup>b</sup>	$\sigma^2$ (Å <sup>2</sup> × 10 <sup>-3</sup> ) <sup>c</sup>	$\Delta E_0$ (eV) <sup>d</sup>	<i>R</i> factor (%)
Pt foil	Pt–Pt	17.6	2.77	5.4	6.7	1.6
PtO <sub>2</sub>	Pt–O	6.0	2.00	1.2	9.9	12.3
Pt <sub>1</sub> /B-TiO <sub>2</sub>	Pt–O	6.4	1.99	3.0	5.6	1.8
	Pt–O	2.0	1.80	4.4		
Pt <sub>1</sub> /TiO <sub>2</sub>	Pt–O	2.5	2.01	6.4	12.3	2.4
Pt <sub>1</sub> Cl <sub>2</sub> /B-TiO <sub>2</sub>	Pt–O	1.9	2.06	28.9	9.8	4.6
	Pt–Pt	0.9	2.75	1.0		
	Pt–Cl	1.7	2.22	28.2		

<sup>a</sup>*N*: coordination numbers; <sup>b</sup>*R*: bond distance; <sup>c</sup> $\sigma^2$ : Debye–Waller factors; <sup>d</sup> $\Delta E_0$ : the inner potential correction. *R* factor: goodness of fit.  $S_0^2$  for Pt–O/Pt–Pt were set as 0.85/0.85. Error bounds (accuracies) obtained by EXAFS spectroscopy were estimated as *N*,  $\pm 20\%$ ;  $\sigma^2$ ,  $\pm 20\%$ ; *R*,  $\pm 0.1$  Å.

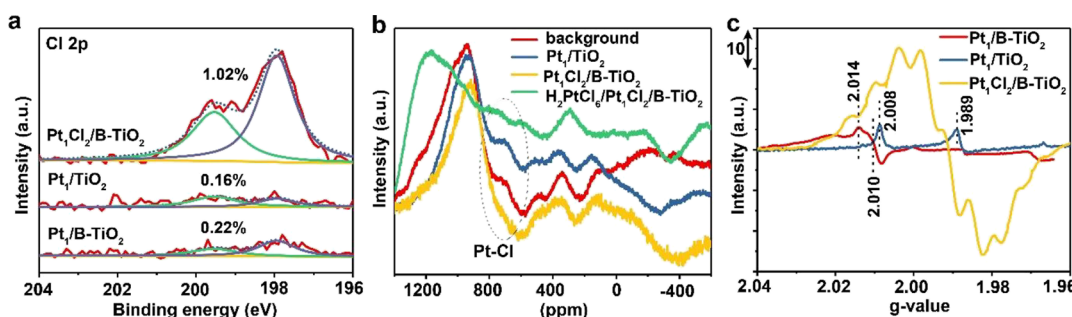


Figure 3. Study of Cl<sup>−</sup> ligands of Pt/TiO<sub>2</sub> catalysts. a, Cl 2p XPS spectra of Pt/TiO<sub>2</sub> catalysts. b, NMR spectra of Pt/TiO<sub>2</sub> catalysts. c, CW EPR spectra of Pt/TiO<sub>2</sub> catalysts measured at 100 K under vacuum.

Raman spectra revealed a phonon mode at 145 cm<sup>−1</sup>, which is an indication of the anatase phase.<sup>40</sup> Compared to that in the spectrum of TiO<sub>2</sub>, the band in the spectrum of Pt<sub>1</sub>/B-TiO<sub>2</sub> shifted to higher wavenumbers, showing that Pt loading causes an increase in oxygen deficiencies in the crystallites of B-TiO<sub>2</sub> (Figure S7). Notably, the peak intensity was reduced in Pt<sub>1</sub>Cl<sub>2</sub>/B-TiO<sub>2</sub>, resulting in nonstoichiometry, defects, and lattice disorders.<sup>41</sup> (Figure S7).

Next, X-ray photoelectron spectroscopy (XPS) was used to identify the Pt<sup>2+</sup> oxidation states of the Pt<sub>1</sub>/B-TiO<sub>2</sub>, Pt<sub>1</sub>/TiO<sub>2</sub>, and Pt<sub>1</sub>Cl<sub>2</sub>/B-TiO<sub>2</sub> catalysts (Figure 2d). X-ray absorption near-edge structure (XANES) analysis (Figure 2e) at the Pt L<sub>3</sub> edge showed that the white line intensities for Pt<sub>1</sub>/B-TiO<sub>2</sub> and Pt<sub>1</sub>/TiO<sub>2</sub> were similar to that of PtO<sub>2</sub>, indicating that the Pt atoms were in a higher oxidation state. The white line intensity for Pt<sub>1</sub>Cl<sub>2</sub>/B-TiO<sub>2</sub> is lower than that of PtO<sub>2</sub> and higher than that of the Pt foil, indicating that the Pt atoms carry a positive charge. The main quantitative structure of the first shell of Pt was characterized with extended X-ray absorption fine structure (EXAFS) spectroscopy. As shown in Figure 2f and Table 1, EXAFS analysis revealed that Pt–O was the only contributor to the Pt<sub>1</sub>/B-TiO<sub>2</sub> and Pt<sub>1</sub>/TiO<sub>2</sub> spectra, confirming the presence of dispersed Pt atoms in Pt<sub>1</sub>/B-TiO<sub>2</sub> and Pt<sub>1</sub>/TiO<sub>2</sub>. The Pt–O bond distance in Pt<sub>1</sub>/TiO<sub>2</sub> was 2.01 Å with a Pt–O coordination number of 2.5, which indicated that Pt–O should be two-coordinate by taking into account the ca. 20% fitting error in EXAFS analysis. However, there were Pt–O contributions at 1.80 Å with a coordination number of 2.0 and 1.99 Å with a coordination number of 6.4 in Pt<sub>1</sub>/B-TiO<sub>2</sub>. The Pt–O coordination number of 6.4 is close to 6.0 of PtO<sub>2</sub> (Table 1), so there is PtO<sub>2</sub> phase in Pt<sub>1</sub>/B-TiO<sub>2</sub>. The PtO<sub>2</sub> phase is attributed to Pt single atom doped into the reduced TiO<sub>2</sub> lattice by replacing the Ti site. It should be noted that Pt has a valence of +2 (Figure 2d) in Pt<sub>1</sub>/B-TiO<sub>2</sub> but Pt has a valence of +4 in PtO<sub>2</sub>, indicating that the PtO<sub>2</sub>

phase in Pt<sub>1</sub>/B-TiO<sub>2</sub> is very little. Therefore, the main Pt–O contribution in Pt<sub>1</sub>/B-TiO<sub>2</sub> is at a distance of 1.80 Å with a coordination number of 2.0. Many oxygen vacancies in reduced TiO<sub>2</sub> induced relaxation of Ti and O atoms, which resulted in a Pt–O coordination at a short distance of 1.80 Å. For Pt<sub>1</sub>Cl<sub>2</sub>/B-TiO<sub>2</sub>, the Pt–O and Pt–Pt bond distances were 2.06 and 2.75 Å, respectively, with a Pt–O coordination number of 1.9 and a Pt–Pt coordination number of 0.9. Careful inspection of the fitted Fourier transform (FT) curves of Pt<sub>1</sub>Cl<sub>2</sub>/B-TiO<sub>2</sub> showed a Pt–Cl bond distance of 2.22 Å with a Pt–Cl average coordination number of 1.7. The two-coordinate Pt–O adopted a four-coordination configuration with the additional two-coordinate Pt–Cl. The identification of Pt–Pt bonds in Pt<sub>1</sub>Cl<sub>2</sub>/B-TiO<sub>2</sub> suggests the presence of Pt nanoparticles, which is in accordance with the STEM results. The Pt–Pt coordination number was low, which indicated the formation of small particles. Generally, Cl<sup>−</sup> ligands on Pt contribute to Pt atom sintering<sup>31–33</sup> so Pt nanoparticles could have been generated in Pt<sub>1</sub>Cl<sub>2</sub>/B-TiO<sub>2</sub>. Furthermore, wavelet transform contour plots based on Morlet wavelets with optimum resolution at the first shell allow qualitative interpretation of Pt–O and Pt–Pt path origins. As shown in Figure S8, the intensity maximum near 5 and 10 Å<sup>−1</sup> is attributed to the Pt–O and Pt–Pt paths, respectively. Both Pt–O and Pt–Pt contributed to Pt<sub>1</sub>Cl<sub>2</sub>/B-TiO<sub>2</sub>, but Pt–O is the main contribution.

**Characterization of Cl<sup>−</sup> Ligands.** The Cl 2p XPS spectra contain two spin-orbit split components, Cl 2p<sub>1/2</sub> located at 199.5 eV and Cl 2p<sub>3/2</sub> located at 197.9 eV (Figure 3a). The intensity of the Cl 2p XPS spectrum of Pt<sub>1</sub>Cl<sub>2</sub>/B-TiO<sub>2</sub> was much higher than those of Pt<sub>1</sub>/TiO<sub>2</sub> and Pt<sub>1</sub>/B-TiO<sub>2</sub>, and the surface Cl ratio in Pt<sub>1</sub>Cl<sub>2</sub>/B-TiO<sub>2</sub> was 1.02%, which is higher than those of Pt<sub>1</sub>/TiO<sub>2</sub> (0.16%) and Pt<sub>1</sub>/B-TiO<sub>2</sub> (0.22%).

To assess the environment around Cl<sup>−</sup> in Pt<sub>1</sub>Cl<sub>2</sub>/B-TiO<sub>2</sub> further, <sup>35</sup>Cl NMR spectroscopy measurements were con-

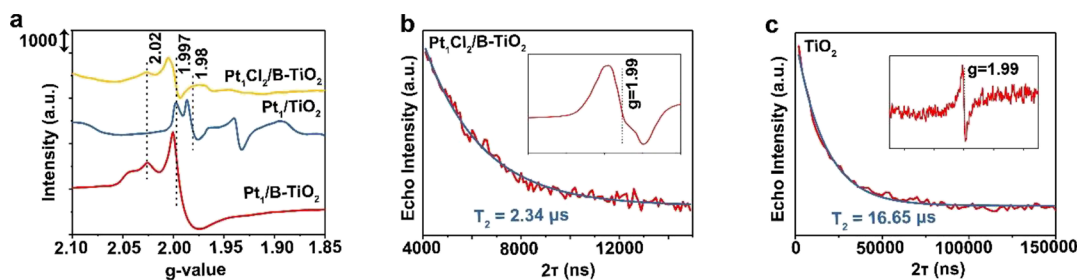


**Figure 4.** EPR measurements of Ti<sup>3+</sup>. **a**, CW EPR spectra of Pt/TiO<sub>2</sub> catalysts measured at 123 K in flowing air. **b**, Two-pulsed EPR spectra of Pt<sub>1</sub>Cl<sub>2</sub>/B-TiO<sub>2</sub> catalysts (red line). Blue line shows a fit to exponential decay with  $T_2 = 2.34 \pm 0.06 \mu\text{s}$ . Inset is the CW EPR spectra of Pt<sub>1</sub>Cl<sub>2</sub>/B-TiO<sub>2</sub> catalysts measured at 6 K. **c**, Two-pulsed EPR spectra of TiO<sub>2</sub> catalysts (red line), and the blue line shows a fit to an exponential decay with  $T_2 = 16.65 \pm 0.37 \mu\text{s}$ . Inset is CW EPR spectra of TiO<sub>2</sub> catalysts measured at 6 K.

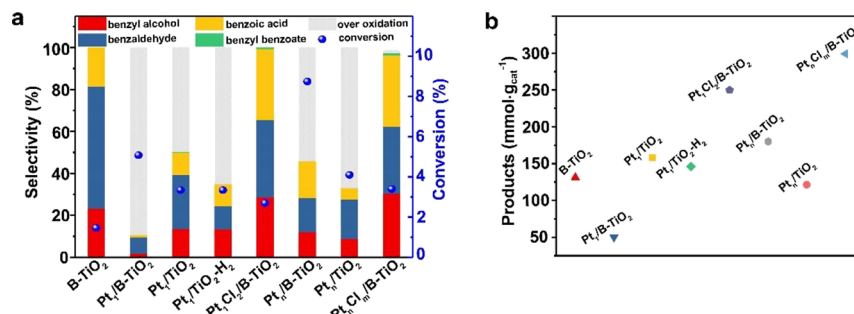


**Figure 5.** Catalytic performance of Pt/TiO<sub>2</sub> catalysts for the selective oxidation of toluene. **a**, Selectivity of the primary C–H oxidation products and conversion of toluene over the Pt/TiO<sub>2</sub> catalysts. **b**, Yield of C–H oxidation products including benzyl alcohol, benzaldehyde, benzoic acid, and benzyl benzoate. Reaction conditions: 1 MPa oxygen, 160 °C, 40 mL toluene, 40 mg catalyst, and 30 h reaction time.

ducted. CDCl<sub>3</sub> was used as the standard reference and yielded a peak at a chemical shift ( $\delta_{\text{iso}}$ ) of 424 ppm. Although the poor signal-to-noise ratio made it challenging to determine the  $\delta_{\text{iso}}$  value of the weak shoulder peak, it was observed between 600 and 800 ppm (Figure S9). In addition, we performed <sup>35</sup>Cl NMR measurements of an empty rotor (background) and tracked changes in the  $\delta_{\text{iso}}$  values of Pt<sub>1</sub>/TiO<sub>2</sub> and Pt<sub>1</sub>Cl<sub>2</sub>/B-TiO<sub>2</sub> that are associated with the Cl chemical environment (Figure 3b). The peaks between 600 and 800 ppm for Pt<sub>1</sub>Cl<sub>2</sub>/B-TiO<sub>2</sub> diminished compared to those of the background and Pt<sub>1</sub>/TiO<sub>2</sub> spectra (Figures 3b, S10 and S11). The H<sub>2</sub>PtCl<sub>6</sub>/Pt<sub>1</sub>Cl<sub>2</sub>/B-TiO<sub>2</sub> mixture, which indeed contains Cl<sup>−</sup> coordination bonds, showed weakened peaks from 600 to 800 ppm compared to those of the background. Thus, the changes in the chemical shifts at 600–800 ppm indicate an increase in the Cl<sup>−</sup> coordination number in Pt<sub>1</sub>Cl<sub>2</sub>/B-TiO<sub>2</sub>.

Figure 3c shows the electron paramagnetic resonance (EPR) spectra of the samples at 100 K under vacuum. This technique was used because EPR spectra are highly sensitive to changes in the structure of Pt–Cl compounds.<sup>42</sup> A resolved hyperfine structure was detected in the EPR spectrum of Pt<sub>1</sub>Cl<sub>2</sub>/B-TiO<sub>2</sub>. As shown in Figure S12, the EPR hyperfine simulation perfectly reproduced the experimental spectrum of Pt<sub>1</sub>Cl<sub>2</sub>/B-TiO<sub>2</sub>, and hyperfine splitting was attributed to the coupling of electron spin with  $I = 3/2$ . The unpaired electron spin constants of <sup>11</sup>B and <sup>35</sup>Cl are both  $I = 3/2$ .<sup>43,44</sup> The absence of a resolved hyperfine structure in the EPR spectrum of B-TiO<sub>2</sub> (Figure S13) and Pt<sub>1</sub>/B-TiO<sub>2</sub> (Figure 3c) demonstrates the absence of B-ion ligands in B-TiO<sub>2</sub>, which could be formed from the reduction of TiO<sub>2</sub> with NaBH<sub>4</sub>. Therefore, the electron spin with  $I = 3/2$  in Pt<sub>1</sub>Cl<sub>2</sub>/B-TiO<sub>2</sub> is attributed to the Cl<sup>−</sup> ligands.

**Semiquantitative Evaluation of Ti<sup>3+</sup>.** Stable Ti<sup>3+</sup> sites are highly active for primary C–H bond activation.<sup>21</sup> Thus, continuous wave EPR (CW EPR) and two-pulsed EPR were used to characterize and semi-quantitatively evaluate, respectively, the Ti<sup>3+</sup> sites. The CW EPR spectra collected at 123 K in flowing air (Figure 4a) of Pt<sub>1</sub>/TiO<sub>2</sub>, Pt<sub>1</sub>/B-TiO<sub>2</sub>, and Pt<sub>1</sub>Cl<sub>2</sub>/B-TiO<sub>2</sub> showed a clear signal with  $g = 1.997$ , which is characteristic of interstitial single Ti<sup>3+</sup> sites that may have been present in the bulk of TiO<sub>2</sub>.<sup>45</sup> Compared to that of Pt<sub>1</sub>/TiO<sub>2</sub>, the intensities of the interstitial Ti<sup>3+</sup> signals for Pt<sub>1</sub>/B-TiO<sub>2</sub> and Pt<sub>1</sub>Cl<sub>2</sub>/B-TiO<sub>2</sub> increased significantly, showing that more interstitial Ti<sup>3+</sup> was present in B-TiO<sub>2</sub>. A remarkable signal with  $g = 1.98$ , attributed to the Ti<sup>3+</sup> regular lattice, was observed for Pt<sub>1</sub>/TiO<sub>2</sub>,<sup>46</sup> but this signal almost disappeared for Pt<sub>1</sub>/B-TiO<sub>2</sub> and Pt<sub>1</sub>Cl<sub>2</sub>/B-TiO<sub>2</sub>, which may be explained by the destruction of the Ti<sup>3+</sup> regular lattice in B-TiO<sub>2</sub>. The signals at  $g = 2.02$  of Pt<sub>1</sub>/B-TiO<sub>2</sub> and Pt<sub>1</sub>Cl<sub>2</sub>/B-TiO<sub>2</sub> correspond to electrons trapped by oxygen vacancies (O<sub>v</sub>).<sup>47</sup> Although the  $g$ -values of the signals corresponding to Ti<sup>3+</sup> and O<sub>v</sub> are slightly different from those obtained at 100 K under vacuum (Figure 3c) because of the influence of temperature and atmosphere, the signals of Pt<sub>1</sub>/TiO<sub>2</sub> and Pt<sub>1</sub>/B-TiO<sub>2</sub> exhibit the same spectral pattern under different temperatures and atmospheres. The CW EPR data indicate interstitial Ti<sup>3+</sup>/O<sub>v</sub> formation and lattice Ti<sup>3+</sup> removal in the B-TiO<sub>2</sub>-supported Pt catalysts, in accordance with the Raman results (Figure S7).

Next, we performed spin-echo experiments with the two-pulsed Hahn echo sequence  $\frac{\pi}{2} - \tau - \pi - \tau - \text{ESE}$  to investigate the spin-echo dephasing time,  $T_2$ . As shown in Figure 4b, c, the curves were best fitted using an exponential function:  $y = A_1 \times \exp\left(-\frac{x}{T_2}\right) + y_0$ . The  $T_2$  values were obtained from the exponential fits, and the  $T_2$  values at 6 K for Pt<sub>1</sub>Cl<sub>2</sub>/B-TiO<sub>2</sub>

and  $\text{TiO}_2$  are 2.34 and  $16.65 \mu\text{s}$ , respectively. As shown in the inset of Figure 4b, the CW EPR spectrum of  $\text{Pt}_1\text{Cl}_2/\text{B}-\text{TiO}_2$  measured at 6 K matches that of the CW EPR spectrum in Figure 4a. The CW EPR spectrum of  $\text{TiO}_2$  shows an axial signal with  $g = 1.99$ , which corresponds to the  $\text{Ti}^{3+}$  sites. (Figure 4c, inset). Thus, considering the concentration of the  $\text{Ti}^{3+}$  spin ( $C_B$ ), we obtained  $\Gamma_{\text{dip}} = 2.53 \frac{\mu_0 g_A g_B \mu_B^2}{4\pi\hbar} C_B$ .  $\Gamma_{\text{dip}}$  is the dipole–dipole interaction between spin A and spin B ( $\text{Ti}^{3+}$ ). We also observed that  $T_2 = 1.4 \sqrt{T_1^B / \Gamma_{\text{dip}}}$ .<sup>48</sup> This indicates that  $T_2$  is inversely proportional to the square root of  $C_B$ . That is, a larger value of  $C_B$  results in a smaller value of  $T_2$ . Because the  $T_2$  value of  $\text{Pt}_1\text{Cl}_2/\text{B}-\text{TiO}_2$  is much smaller than that of  $\text{TiO}_2$ , this semiquantitative evaluation of  $\text{Ti}^{3+}$  indicates that there are more  $\text{Ti}^{3+}$  species in  $\text{Pt}_1\text{Cl}_2/\text{B}-\text{TiO}_2$  than in  $\text{TiO}_2$ .

The characterization of  $\text{Cl}^-$  ligands and  $\text{Ti}^{3+}$  sites indicates that  $\text{Cl}^-$  ligands bonded to the single Pt atoms probably formed four-coordinate  $\text{Pt}_1$  sites and that  $\text{Pt}_1\text{Cl}_2/\text{B}-\text{TiO}_2$  contained more  $\text{Ti}^{3+}$  sites. Furthermore, the DFT calculations (Figure 1) indicate that the four-coordinate  $\text{Pt}_1$  sites are inactive for oxygen activation to facilitate toluene oxidation, so the over-oxidation of toluene can be avoided on  $\text{Pt}_1\text{Cl}_2/\text{B}-\text{TiO}_2$ .

**Catalytic Performance of  $\text{Pt}_1\text{Cl}_2/\text{B}-\text{TiO}_2$ .** When testing the catalysts for the selective oxidation of toluene, the selective primary C–H oxidation products were benzyl alcohol, benzaldehyde, benzoic acid, and benzyl benzoate. As shown in Figure 5a, the selectivities over  $\text{Pt}_1/\text{B}-\text{TiO}_2$  and  $\text{Pt}_1/\text{TiO}_2$  were 10.6 and 50.1%, respectively. The lower selectivities of  $\text{Pt}_1/\text{B}-\text{TiO}_2$  and  $\text{Pt}_1/\text{TiO}_2$  are attributed to the over-oxidation of toluene on the two-coordinate  $\text{Pt}_1$  sites. It is noted that the conversion of toluene on  $\text{Pt}_1/\text{B}-\text{TiO}_2$  is 5.08%, 3.5 times higher than that obtained over  $\text{B}-\text{TiO}_2$ . The high conversion on  $\text{Pt}_1/\text{B}-\text{TiO}_2$  is attributed to the remarkable conversion of toluene to over-oxidation products over  $\text{Pt}_1$  sites on  $\text{Pt}_1/\text{B}-\text{TiO}_2$ , and thus, the selective oxidation of the primary C–H bond was inhibited and resulted in a low selectivity. The selectivity of the C–H oxidation products over both  $\text{B}-\text{TiO}_2$  and  $\text{Pt}_1\text{Cl}_2/\text{B}-\text{TiO}_2$  is 100%. The over-oxidation of toluene is inhibited due to the inactivation of four-coordinate  $\text{Pt}_1$  sites in  $\text{Pt}_1\text{Cl}_2/\text{B}-\text{TiO}_2$ . Furthermore, the conversion of toluene over  $\text{B}-\text{TiO}_2$  is lower than that over  $\text{Pt}_1\text{Cl}_2/\text{B}-\text{TiO}_2$ , which is attributed to more interfacial  $\text{Ti}^{3+}$  sites stabilized by Pt atoms under the reaction conditions in  $\text{Pt}_1\text{Cl}_2/\text{B}-\text{TiO}_2$ .

Furthermore, the effect of pretreatment conditions on the catalytic behaviors was investigated. XPS results identified the  $\text{Pt}^{2+}$  oxidation states of  $\text{Pt}_1/\text{TiO}_2-\text{H}_2$ , which implied the generation of  $\text{Pt}_1$  sites (Figure S14a). The surface Cl ratio in  $\text{Pt}_1/\text{TiO}_2-\text{H}_2$  was 0.29% (Figure S14b), which is higher than 0.16% in  $\text{Pt}_1/\text{TiO}_2$  but much lower than 1.02% in  $\text{Pt}_1\text{Cl}_2/\text{B}-\text{TiO}_2$  (Figure 3a). It is difficult to adopt four-coordination  $\text{Pt}_1$  sites with  $\text{Cl}^-$  ligation in  $\text{Pt}_1/\text{TiO}_2-\text{H}_2$  due to the low surface Cl ratio. Thus, the selectivity of the C–H oxidation products was 34.7% over  $\text{Pt}_1/\text{TiO}_2-\text{H}_2$ , which is attributed to conversion of toluene to over oxidation products on  $\text{Pt}_1$  sites. Moreover, part of  $\text{TiO}_2$  would turn into reduced- $\text{TiO}_2$  after  $\text{H}_2$  reduction treatment, so part of  $\text{Pt}_1/\text{TiO}_2-\text{H}_2$  was in fact  $\text{Pt}_1/\text{B}-\text{TiO}_2$ . Because  $\text{Pt}_1/\text{B}-\text{TiO}_2$  showed the lowest selectivity, the selectivity over  $\text{Pt}_1/\text{TiO}_2-\text{H}_2$  was lower than that over  $\text{Pt}_1/\text{TiO}_2$ .

The yield of the primary C–H bond oxidation products based on per gram catalyst could be used to compare the

catalytic performance of different catalysts. As shown in Figure 5b and Table S3, the higher yield over the  $\text{Pt}_1\text{Cl}_2/\text{B}-\text{TiO}_2$  catalyst than that over  $\text{Pt}_1/\text{B}-\text{TiO}_2$  and  $\text{Pt}_1/\text{TiO}_2$  was attributed to the enhanced selectivity of the C–H oxidation products. The yield of the C–H oxidation products over the  $\text{Pt}_1\text{Cl}_2/\text{B}-\text{TiO}_2$  catalyst was  $249.8 \text{ mmol g}_{\text{cat}}^{-1}$ , 1.9 times higher than that obtained over our reported N-doped  $\text{TiO}_2$  catalyst ( $132.8 \text{ mmol g}_{\text{cat}}^{-1}$ )<sup>20</sup> and 4.2 times higher than that obtained for a reported  $\text{AuPd}/\text{TiO}_2$  catalyst ( $59.5 \text{ mmol g}_{\text{cat}}^{-1}$ ).<sup>29</sup>

$\text{O}_2^-$  radicals can initiate the selective oxidation of toluene.<sup>20,29</sup> Here, the  $\text{O}_2^-$  radical scavenger experiment was performed by adding p-benzoquinone. The results showed that the yield and selectivity over  $\text{Pt}_1\text{Cl}_2/\text{B}-\text{TiO}_2$ , respectively, decreased to  $122 \text{ mmol g}_{\text{cat}}^{-1}$  and 27.9%, when added 50 mg of p-benzoquinone (Figures S15 and S16). The yield and selectivity, respectively, decreased to  $51 \text{ mmol g}_{\text{cat}}^{-1}$  and 13.1%, when added 80 mg of p-benzoquinone. It indicated that the activation of oxygen to generate  $\text{O}_2^-$  radicals was the key step in the primary C–H bond oxidation of toluene.

Single Pt atoms were the main Pt dispersion in  $\text{Pt}_1\text{Cl}_2/\text{B}-\text{TiO}_2$ , but a few Pt nanoparticles were observed due to  $\text{Cl}^-$  ligand contribution to Pt atom sintering according to STEM (Figures 2c and S5) and wavelet transform results (Figure S8). To investigate the effect of platinum dispersion on the catalytic performance, Pt nanoparticle catalysts, namely,  $\text{Pt}_n/\text{B}-\text{TiO}_2$ ,  $\text{Pt}_n/\text{TiO}_2$ , and  $\text{Pt}_n\text{Cl}_m/\text{B}-\text{TiO}_2$  were synthesized. HAADF-STEM (Figure S17), Pt L-edge XANES (Figure S18), EXAFS in R space (Figure S19 and Table S4), and wavelet transform contour plots (Figure S20) indicated the generation of Pt nanoparticles in three Pt nanoparticle catalysts and a Pt–Cl coordination contribution in  $\text{Pt}_n\text{Cl}_m/\text{B}-\text{TiO}_2$  (see the discussion in the Supporting Information). As shown in Figure 5 and Table S3, the selectivity of  $\text{Pt}_n/\text{B}-\text{TiO}_2$  and  $\text{Pt}_n/\text{TiO}_2$  was 45.7 and 32.9%, respectively, and the selectivity of  $\text{Pt}_n\text{Cl}_m/\text{B}-\text{TiO}_2$  was 97.2%. It indicated that the over-oxidation of toluene was significantly inhibited due to  $\text{Cl}^-$  ligation on Pt nanoparticles. Furthermore, the conversion of toluene over  $\text{Pt}_n\text{Cl}_m/\text{B}-\text{TiO}_2$  was 3.40%, which is higher than 2.70% obtained over  $\text{Pt}_1\text{Cl}_2/\text{B}-\text{TiO}_2$ . Thus, the yield of the C–H oxidation products over the  $\text{Pt}_n\text{Cl}_m/\text{B}-\text{TiO}_2$  reaches  $299.0 \text{ mmol g}_{\text{cat}}^{-1}$ . However, the over-oxidation over  $\text{Pt}_n\text{Cl}_m/\text{B}-\text{TiO}_2$  was not inhibited completely. Compared to the Cl ratio of 1.02% in  $\text{Pt}_1\text{Cl}_2/\text{B}-\text{TiO}_2$ , the Cl ratio of  $\text{Pt}_n\text{Cl}_m/\text{B}-\text{TiO}_2$  decreased to 0.42% due to higher temperature calcination (Figure S21). The coordination of  $\text{Cl}^-$  ligation on Pt nanoparticles was not further studied because the configuration of Pt nanoparticle is difficult to construct.

## CONCLUSIONS

Chloride ligands coordinated to single Pt atoms had a strong effect on the catalytic selectivity in a system where reduced metal sites in the catalyst support are the catalytically active sites and Pt causes over-oxidation. In such systems, catalyst design is particularly important. Crucially, reduced  $\text{TiO}_2$ -supported Pt single atoms were fabricated, where the transfer of electrons from Pt to  $\text{Ti}^{3+}$  is difficult. In contrast, the strong electronic interactions between the Pt atoms and  $\text{Cl}^-$  ligands causes the formation of strong Pt–Cl bonds, which lead to Pt single atom inactivation and thus enhanced the selectivity of the primary C–H bond oxidation. Furthermore, many  $\text{Ti}^{3+}$  sites in reduced  $\text{TiO}_2$  stabilized with electron-rich Pt atoms could increase the activity for the primary C–H bond oxidation of toluene. As a result,  $\text{Pt}_1\text{Cl}_2/\text{B}-\text{TiO}_2$  achieved a

yield of the primary C–H bond oxidation products of 249.8 mmol g<sub>cat</sub><sup>-1</sup>. The addition of Cl<sup>-</sup> ligands on noble metal catalysts is expected to be an effective method for the preparation of efficient catalysts for catalytic selective oxidation reactions.

## ■ EXPERIMENTAL SECTION

**Synthesis of Reduced-TiO<sub>2</sub> Catalysts.** Reduced-TiO<sub>2</sub> was synthesized using a reduction method. Briefly, equal masses of commercial TiO<sub>2</sub> (anatase, Sigma–Aldrich) and NaBH<sub>4</sub> were ground to form a homogeneous mixture, and this was heated in N<sub>2</sub> flow at 260 °C for 2 h. The as-prepared powder was then washed with ethanol and ultrapure water several times. The obtained samples were then dried at 60 °C for 12 h, and the reduced TiO<sub>2</sub> samples are denoted “B-TiO<sub>2</sub>.”

**Synthesis of the Pt<sub>1</sub>/B-TiO<sub>2</sub> and Pt<sub>n</sub>/B-TiO<sub>2</sub> Catalyst.** The Pt<sub>1</sub>/B-TiO<sub>2</sub> catalyst was synthesized using an electrostatic adsorption method. To synthesize a 0.15 wt % Pt<sub>1</sub>/B-TiO<sub>2</sub> catalyst, ultrapure water (25 mL) was mixed with ammonium hydroxide (75 mL) to dissolve the TiO<sub>2</sub> support (1 g, anatase, Sigma–Aldrich) to yield a suspension. The pH of the suspension was maintained at 12. Next, tetraammineplatinum(II) chloride (50 mg, TAPC, PtCl<sub>2</sub>·4(NH<sub>3</sub>)·H<sub>2</sub>O) (Sigma–Aldrich) was dissolved in ultrapure water (25 mL) to prepare a TAPC solution, and this solution (1.284 mL) was added to ammonium hydroxide (25 mL) to create a TAPC precursor solution with a pH value of 12. Subsequently, the TAPC precursor solution (25 mL) was injected into the TiO<sub>2</sub> support suspension (100 mL) at a rate of 2 mL/h with constant stirring to achieve a final total volume of 125 mL. Subsequently, the final suspension was heated to 70 °C until the liquid had evaporated completely. Finally, the Pt/TiO<sub>2</sub> sample was calcined in He gas at 200 °C for 4 h, followed by H<sub>2</sub> reduction at 200 °C for 4 h.

The synthesis of Pt<sub>n</sub>/B-TiO<sub>2</sub> catalyst was the same with the Pt<sub>1</sub>/B-TiO<sub>2</sub> catalyst, but calcined in He gas at 600 °C for 4 h, followed by H<sub>2</sub> reduction at 600 °C for 4 h.

**Synthesis of the Pt<sub>1</sub>/TiO<sub>2</sub> and Pt<sub>n</sub>/TiO<sub>2</sub> Catalyst.** The Pt<sub>1</sub>/TiO<sub>2</sub> catalyst was synthesized using a wet impregnation method. H<sub>2</sub>PtCl<sub>6</sub> was chosen as the platinum precursor, and TiO<sub>2</sub> (1 g, anatase, Sigma–Aldrich) was added to H<sub>2</sub>PtCl<sub>6</sub> solution (1 mL, 7.69 mol mL<sup>-1</sup>), followed by impregnation for 12 h. The slurry was washed several times with ultrapure water and then dried at 60 °C for 6 h. The as-prepared powder was calcined at 200 °C in a muffle furnace for 4 h.

The synthesis of the Pt<sub>n</sub>/TiO<sub>2</sub> catalyst was the same with Pt<sub>1</sub>/TiO<sub>2</sub> but calcined at 600 °C in a muffle furnace for 4 h.

**Synthesis of the Pt<sub>1</sub>/TiO<sub>2</sub>–H<sub>2</sub> Catalyst.** Briefly, the Pt<sub>1</sub>/TiO<sub>2</sub>–H<sub>2</sub> catalyst was synthesized using the wet impregnation method, and the procedures were the same with Pt<sub>1</sub>/TiO<sub>2</sub>, but calcined at 200 °C in He gas for 4 h, followed by H<sub>2</sub> reduction at 200 °C for 4 h.

**Synthesis of the Pt<sub>1</sub>Cl<sub>2</sub>/B-TiO<sub>2</sub> and Pt<sub>n</sub>Cl<sub>m</sub>/B-TiO<sub>2</sub> Catalyst.** The Pt<sub>1</sub>Cl<sub>2</sub>/B-TiO<sub>2</sub> catalyst was also synthesized using the wet impregnation method, and the procedures were the same to those used for the Pt<sub>1</sub>/TiO<sub>2</sub>–H<sub>2</sub> catalyst, except that B-TiO<sub>2</sub> was used as the support.

The synthesis of the Pt<sub>n</sub>Cl<sub>m</sub>/B-TiO<sub>2</sub> catalyst was the same procedure with Pt<sub>1</sub>Cl<sub>2</sub>/B-TiO<sub>2</sub>, but calcined in He gas at 600 °C for 4 h, followed by H<sub>2</sub> reduction at 600 °C for 4 h.

**Computational Analysis.** All calculations were performed using periodic DFT in the Vienna ab initio simulation package (VASP). The projector-augmented wave method was used to model the interactions between the core and valence electrons. The valence orbitals of Ti (3p, 4s, 3d), Pt (5d, 6s), O (2s, 2p), C (2s, 2p), and H (1s) were described using plane-wave basis sets with cutoff energies of 400 eV. The exchange–correlation energy was approximated using the generalized gradient approximation Perdew–Burke–Ernzerhof functional. The convergence criteria for the energies and forces were set to 10<sup>-5</sup> eV and 0.02 eV Å<sup>-1</sup>, respectively. Spin polarization was also included.

The anatase TiO<sub>2</sub> (001) surface was modeled as periodic slabs of six layers (i.e., six Ti planes) and a vacuum layer of approximately 15 Å. A 3 × 3 surface supercell was used, and the bottom two layers were fixed to their bulk positions. The Brillouin zone was sampled only by the  $\Gamma$ -point during all calculations. The Pt(111) surface was modeled using a 2 × 2 supercell with four layers of Pt atoms, and the bottom two layers were fixed during all the calculations. A vacuum layer of thickness 15 Å was used. The adsorption energies ( $E_{\text{ads}}$ ) of the gas molecules were calculated as follows:  $E_{\text{ads}} = E_{\text{gas+M1/DG}} - E_{\text{M1/DG}} - E_{\text{gas}}$ .

**Characterization.** HAADF-STEM imaging was performed using a JEM-ARM 200F electron microscope equipped with two spherical aberration correctors. Measurements were performed at an acceleration voltage of 300 kV. Pt L<sub>3</sub>-edge EXAFS spectra were measured at the IW1B beamline of the Beijing Synchrotron Radiation Facility (BSRF), which was operated at approximately 200 mA and 2.2 GeV. Pt foil and PtO<sub>2</sub> were used as reference samples. The Pt foil and PtO<sub>2</sub> samples were analyzed in transmission mode. The Pt K-edges of Pt/TiO<sub>2</sub> and Pt/B-TiO<sub>2</sub> were measured using a solid-state detector. XPS measurements were performed using an Axis Supra system with a monochromatic Al K<sub>α</sub> standard radiation source. The binding energies were calibrated against the adventitious C 1s peak (284.8 eV).

CW EPR at 123 K in flowing air were performed on a JEOL-FA200 spectrometer with 100 kHz magnetic field modulation. CW EPR at 100 K under vacuum was performed on a Chinainstru & Quantumtech (Hefei) EPR-100 spectrometer with 100 kHz magnetic field modulation. Pulsed EPR was carried out on a Chinainstru & Quantumtech (Hefei) EPR-100 spectrometer equipped with a cryogen-free EPR variable temperature systems operating at 6 K. The ESE-detected EPR spectra were recorded using a standard Hahn echo pulse sequence:  $\frac{\pi}{2} - \tau - \pi - \tau - \text{ESE}$  with a  $\frac{\pi}{2}$  pulse length of 15 ns and  $\tau = 400 + n \times 50$  ns.

<sup>35</sup>Cl NMR experiments were performed in a magnetic field of 14.1 T using a JEOL JNM-ECZ600R spectrometer equipped with a triple-channel 8-mm probe at a spinning frequency of 5 kHz. The chemical shifts corresponding to <sup>35</sup>Cl were referenced to CDCl<sub>3</sub>. <sup>35</sup>Cl NMR data of Pt<sub>1</sub>/TiO<sub>2</sub> and Pt<sub>1</sub>Cl<sub>2</sub>/B-TiO<sub>2</sub> were recorded in the range of -0.6 to 1.4 ppt with 60,000 scans and 52,000 scans, respectively, with an echo delay time of 1 s. We repeated the experiment on an empty rotor, and the data are shown as the background. The <sup>35</sup>Cl NMR data of a mixture of H<sub>2</sub>PtCl<sub>6</sub> and Pt<sub>1</sub>Cl<sub>2</sub>/B-TiO<sub>2</sub> were also recorded using 52,000 scans. The <sup>35</sup>Cl NMR data for an empty rotor and Pt<sub>1</sub>Cl<sub>2</sub>/B-TiO<sub>2</sub> were verified by repeating the experiments from 0.5 to 1, 0 to 0.5, -0.5 to 0, and -1 to -0.5 ppt with 13,000 × 4 scans.

**Catalytic Activity Tests.** The primary C–H oxidation of toluene was performed in an autoclave (100 mL). The vessel was charged with the desired amounts of toluene (40 mL) and catalyst (40 mg). The autoclave was purged five times with O<sub>2</sub> at 0.5 MPa and then filled with O<sub>2</sub> at 1 MPa. The stirring speed was set at 1500 rpm, and the reaction mixture was heated to 160 °C. The reaction liquid was collected from the reactor after a reaction time of 30 h using a sampling system. *o*-Xylene (0.5 mL) was added to the reaction liquid (0.5 mL) as an internal standard. The reactants and products were analyzed using a gas chromatography (Agilent 7890A) system equipped with an on-column injector, flame ionization detector (FID), and a CP-Wax 52 CB column. The conversion rate and selectivity were calculated using the following equations:

$$\text{Total selectivity (\%)} = \frac{M + \text{benzyl benzoate (mmol)} \times 2}{\text{toluene conversion (mmol)}} \times 100\%$$

where  $M = [\text{benzyl alcohol (mmol)}] + [\text{benzaldehyde (mmol)}] + [\text{benzoic acid (mmol)}]$ .

The O<sub>2</sub><sup>-</sup> radical scavenger experiment was performed by adding p-benzoquinone (50 or 80 mg) together with the catalyst. The reactants and products were analyzed to study the effect of -O<sub>2</sub><sup>-</sup> radical on selective oxidation of toluene.

## ASSOCIATED CONTENT

### Supporting Information

The Supporting Information is available free of charge at <https://pubs.acs.org/doi/10.1021/jacs.3c03257>.

Additional DFT calculations and supplementary characterization results of  $\text{TiO}_2$ ; B- $\text{TiO}_2$  and supported single Pt atom catalysts, including STEM, XRD, Raman, wavelet transforms, NMR, EPR simulator, CW EPR, XPS, catalytic results; characterization results and discussion of supported Pt nanoparticle catalysts, including STEM, XANES, EXAFS fittings, wavelet transforms, and XPS results; and reported toluene oxidation activity (PDF)

## AUTHOR INFORMATION

### Corresponding Authors

Hai Xiao – Department of Chemistry, Tsinghua University, Beijing 100084, China; [orcid.org/0000-0001-9399-1584](https://orcid.org/0000-0001-9399-1584); Phone: +86-10-62786113; Email: [haixiao@tsinghua.edu.cn](mailto:haixiao@tsinghua.edu.cn)

Maoyong Song – Key Laboratory of Environmental Nanotechnology and Health Effects, Research Center for Eco-Environmental Sciences, Chinese Academy of Sciences, Beijing 100085, China; University of Chinese Academy of Sciences, Beijing 100049, China; [orcid.org/0000-0002-6776-4705](https://orcid.org/0000-0002-6776-4705); Phone: +86-10-62918178; Email: [mysong@rcees.ac.cn](mailto:mysong@rcees.ac.cn)

### Authors

Chunyan Ma – Key Laboratory of Environmental Nanotechnology and Health Effects, Research Center for Eco-Environmental Sciences, Chinese Academy of Sciences, Beijing 100085, China; University of Chinese Academy of Sciences, Beijing 100049, China

Chenggong Yang – Key Laboratory of Environmental Nanotechnology and Health Effects, Research Center for Eco-Environmental Sciences, Chinese Academy of Sciences, Beijing 100085, China; University of Chinese Academy of Sciences, Beijing 100049, China

Hongying Zhuo – Department of Chemistry, Tsinghua University, Beijing 100084, China

Cheng Chen – Key Laboratory of Environmental Nanotechnology and Health Effects, Research Center for Eco-Environmental Sciences, Chinese Academy of Sciences, Beijing 100085, China; University of Chinese Academy of Sciences, Beijing 100049, China

Ke Lu – Department of Chemistry, Tsinghua University, Beijing 100084, China

Fengbang Wang – Key Laboratory of Environmental Nanotechnology and Health Effects, Research Center for Eco-Environmental Sciences, Chinese Academy of Sciences, Beijing 100085, China; University of Chinese Academy of Sciences, Beijing 100049, China; [orcid.org/0000-0001-5518-6111](https://orcid.org/0000-0001-5518-6111)

Zhifu Shi – Chinainstru & Quantumtech (Hefei) Co., Ltd, Hefei 230031, China

Guibin Jiang – State Key Laboratory of Environmental Chemistry and Ecotoxicology, Research Center for Eco-Environmental Sciences, Chinese Academy of Sciences, Beijing 100085, China; University of Chinese Academy of Sciences, Beijing 100049, China; [orcid.org/0000-0002-6335-3917](https://orcid.org/0000-0002-6335-3917)

Complete contact information is available at: <https://pubs.acs.org/doi/10.1021/jacs.3c03257>

## Notes

The authors declare no competing financial interest.

## ACKNOWLEDGMENTS

This work was supported by the National Natural Science Foundation of China (grants 22125606, 21976198, 21777175).

## REFERENCES

- 1) Armstrong, R. D.; Hirayama, J.; Knight, D. W.; Hutchings, G. J. Quantitative Determination of Pt-Catalyzed d-Glucose Oxidation Products Using 2D NMR. *ACS Catal.* **2018**, *9*, 325–335.
- 2) Ait Rass, H.; Essayem, N.; Besson, M. Selective aerobic oxidation of 5-HMF into 2,5-furandicarboxylic acid with Pt catalysts supported on  $\text{TiO}_2$ - and  $\text{ZrO}_2$ -based supports. *ChemSusChem* **2015**, *8*, 1206–1217.
- 3) Durndell, L. J.; Isaacs, M. A.; Li, C. E.; Parlett, C. M. A.; Wilson, K.; Lee, A. F. Cascade Aerobic Selective Oxidation over Contiguous Dual-Catalyst Beds in Continuous Flow. *ACS Catal.* **2019**, *9*, 5345–5352.
- 4) Mahlaba, S. V. L.; Hytoolakhan Lal Mahomed, N.; Govender, A.; Guo, J.; Leteba, G. M.; Cilliers, P. L.; van Steen, E. Platinum-Catalysed Selective Aerobic Oxidation of Methane to Formaldehyde in the Presence of Liquid Water. *Angew. Chem.* **2022**, *61*, No. e202206841.
- 5) Yan, H.; He, K.; Samek, I. A.; Jing, D.; Nanda, M. G.; Stair, P. C.; Notestein, J. M. Tandem  $\text{In}_2\text{O}_3$ -Pt/ $\text{Al}_2\text{O}_3$  catalyst for coupling of propane dehydrogenation to selective  $\text{H}_2$  combustion. *Science* **2021**, *371*, 1257–1260.
- 6) Jiang, F.; Zeng, L.; Li, S.; Liu, G.; Wang, S.; Gong, J. Propane Dehydrogenation over  $\text{Pt}/\text{TiO}_2$ - $\text{Al}_2\text{O}_3$  Catalysts. *ACS Catal.* **2014**, *5*, 438–447.
- 7) Wang, C.; Mao, S.; Wang, Z.; Chen, Y.; Yuan, W.; Ou, Y.; Zhang, H.; Gong, Y.; Wang, Y.; Mei, B.; Jiang, Z.; Wang, Y. Insight into Single-Atom-Induced Unconventional Size Dependence over  $\text{CeO}_2$ -Supported Pt Catalysts. *Chem.* **2020**, *6*, 752–765.
- 8) Zhang, Z.; Zhu, Y.; Asakura, H.; Zhang, B.; Zhang, J.; Zhou, M.; Han, Y.; Tanaka, T.; Wang, A.; Zhang, T.; Yan, N. Thermally stable single atom Pt/m- $\text{Al}_2\text{O}_3$  for selective hydrogenation and CO oxidation. *Nat. Commun.* **2017**, *8*, 16100.
- 9) Su, J.; Xie, C.; Chen, C.; Yu, Y.; Kennedy, G.; Somorjai, G. A.; Yang, P. Insights into the Mechanism of Tandem Alkene Hydroformylation over a Nanostructured Catalyst with Multiple Interfaces. *J. Am. Chem. Soc.* **2016**, *138*, 11568–11574.
- 10) Zhang, B.; Sun, G.; Ding, S.; Asakura, H.; Zhang, J.; Sautet, P.; Yan, N. Atomically Dispersed  $\text{Pt}_1$ -Polyoxometalate Catalysts: How Does Metal-Support Interaction Affect Stability and Hydrogenation Activity? *J. Am. Chem. Soc.* **2019**, *141*, 8185–8197.
- 11) Fu, J.; Lym, J.; Zheng, W.; Alexopoulos, K.; Mironenko, A. V.; Li, N.; Boscoboinik, J. A.; Su, D.; Weber, R. T.; Vlachos, D. G. C–O bond activation using ultralow loading of noble metal catalysts on moderately reducible oxides. *Nat. Catal.* **2020**, *3*, 446–453.
- 12) Wang, Z.; Wang, C.; Mao, S.; Lu, B.; Chen, Y.; Zhang, X.; Chen, Z.; Wang, Y. Decoupling the electronic and geometric effects of Pt catalysts in selective hydrogenation reaction. *Nat. Commun.* **2022**, *13*, 3561.
- 13) Phan, D.-P.; Le, V. N.; Nguyen, T. H.; Kim, H. B.; Park, E. D.; Kim, J.; Lee, E. Y. Effect of amino-defective-MOF materials on the selective hydrodeoxygenation of fatty acid over Pt-based catalysts. *J. Catal.* **2021**, *400*, 283–293.
- 14) Schoenbaum, C. A.; Schwartz, D. K.; Medlin, J. W. Controlling the surface environment of heterogeneous catalysts using self-assembled monolayers. *Acc. Chem. Res.* **2014**, *47*, 1438–1445.
- 15) Lu, L.; Zou, S.; Fang, B. The critical impacts of ligands on heterogeneous nanocatalysis: A review. *ACS Catal.* **2021**, *11*, 6020–6058.
- 16) Makosch, M.; Lin, W.-I.; Bumbálek, V.; Sá, J.; Medlin, J. W.; Hungerbühler, K.; van Bokhoven, J. A. Organic thiol modified Pt/

- TiO<sub>2</sub> catalysts to control chemoselective hydrogenation of substituted nitroarenes. *ACS Catal.* **2012**, *2*, 2079–2081.
- (17) Yang, P.; Pan, J.; Liu, Y.; Zhang, X.; Feng, J.; Hong, S.; Li, D. Insight into the role of unsaturated coordination O<sub>2c</sub>-Ti<sub>5c</sub>-O<sub>2c</sub> sites on selective glycerol oxidation over AuPt/TiO<sub>2</sub> catalysts. *ACS Catal.* **2019**, *9*, 188–199.
- (18) Liu, N.; Xu, M.; Yang, Y.; Zhang, S.; Zhang, J.; Wang, W.; Zheng, L.; Hong, S.; Wei, M. Au<sup>δ+</sup>-O<sub>v</sub>-Ti<sup>3+</sup> interfacial site: Catalytic active center toward low-temperature water gas shift reaction. *ACS Catal.* **2019**, *9*, 2707–2717.
- (19) Kennedy, G.; Baker, L. R.; Somorjai, G. A. Selective amplification of C=O bond hydrogenation on Pt/TiO<sub>2</sub>: catalytic reaction and sum-frequency generation vibrational spectroscopy studies of crotonaldehyde hydrogenation. *Angew. Chem., Int. Ed.* **2014**, *53*, 3405–3408.
- (20) Chen, C.; Wu, M.; Yang, C.; Yu, X.; Yu, J.; Yin, H.; Li, G.; Su, G.; Hao, Z.; Song, M.; Ma, C. Electron-donating N<sup>+</sup>-Ti<sup>3+</sup>-O<sub>v</sub> interfacial sites with high selectivity for the oxidation of primary C–H bonds. *Cell Rep. Phys. Sci.* **2022**, *3*, No. 100936.
- (21) Ma, B.; Zhang, Z.; Song, W.; Xue, X.; Yu, Y.; Zhao, Z.; Ding, Y. Solvent-free selective oxidation of C–H bonds of toluene and substituted toluene to aldehydes by vanadium-substituted polyoxometalate catalyst. *J. Mol. Catal. A: Chem.* **2013**, *368–369*, 152–158.
- (22) Xia, H.; Liu, Z.; Xu, Y.; Zuo, J.; Qin, Z. Highly efficient V-Mo-Fe-O catalysts for selective oxidation of toluene to benzaldehyde. *Catal. Commun.* **2016**, *86*, 72–76.
- (23) Mal, D. D.; Khilari, S.; Pradhan, D. Efficient and selective oxidation of toluene to benzaldehyde on manganese tungstate nanobars: a noble metal-free approach. *Green Chem.* **2018**, *20*, 2279–2289.
- (24) Han, H.; Ding, G.; Wu, T.; Yang, D.; Jiang, T.; Han, B. Cu and boron doped carbon nitride for highly selective oxidation of toluene to benzaldehyde. *Molecules* **2015**, *20*, 12686–12697.
- (25) Acharyya, S. S.; Ghosh, S.; Tiwari, R.; Sarkar, B.; Singha, R. K.; Pendem, C.; Sasaki, T.; Bal, R. Preparation of the CuCr<sub>2</sub>O<sub>4</sub> spinel nanoparticles catalyst for selective oxidation of toluene to benzaldehyde. *Green Chem.* **2014**, *16*, 2500–2508.
- (26) Shi, G.; Xu, S.; Bao, Y.; Xu, J.; Liang, Y. Selective aerobic oxidation of toluene to benzaldehyde on immobilized CoO<sub>x</sub> on SiO<sub>2</sub> catalyst in the presence of N-hydroxyphthalimide and hexafluoropropan-2-ol. *Catal. Commun.* **2019**, *123*, 73–78.
- (27) Wu, X.; Deng, Z.; Yan, J.; Zhang, F.; Zhang, Z. Effect of acetic anhydride on the oxidation of toluene to benzaldehyde with metal/bromide catalysts. *Ind. Eng. Chem. Res.* **2014**, *53*, 14601–14606.
- (28) Fu, B.; Zhu, X.; Xiao, G. Solvent-free selective aerobic oxidation of toluene by ultra fine nano-palladium catalyst. *Appl. Catal., A* **2012**, *415–416*, 47–52.
- (29) Kesavan, L.; Tiruvalam, R.; Rahim, M. H. A.; Saiman, M. I. B.; Enache, D. I.; Jenkins, R. L.; Dimitratos, N.; Lopez-Sanchez, J. A.; Taylor, S. H.; Knight, D. W.; Kiely, C. J.; Hutching, G. J. Solvent-free oxidation of primary carbon-hydrogen bonds in toluene using Au-Pd alloy nanoparticles. *Science* **2011**, *331*, 195–199.
- (30) Zhou, Y.; Doronkin, D. E.; Chen, M.; Wei, S.; Grunwaldt, J.-D. Interplay of Pt and crystal facets of TiO<sub>2</sub>: CO oxidation activity and operando XAS/DRIFTS studies. *ACS Catal.* **2016**, *6*, 7799–7809.
- (31) Oenema, J.; van Alst, R. A.; Meijerink, M. J.; Zečević, J.; de Jong, K. P. The influence of residual chlorine on Pt/Zeolite Y/γ-Al<sub>2</sub>O<sub>3</sub> composite catalysts: acidity and performance. *Appl. Catal., A* **2020**, *605*, No. 117815.
- (32) Oran, U.; Uner, D. Mechanisms of CO oxidation reaction and effect of chlorine ions on the CO oxidation reaction over Pt/CeO<sub>2</sub> and Pt/CeO<sub>2</sub>/γ-Al<sub>2</sub>O<sub>3</sub> catalysts. *Appl. Catal., B* **2004**, *54*, 183–191.
- (33) Karhu, H.; Kalantar, A.; Väyrynen, I. J.; Salmi, T.; Murzin, D. Y. XPS analysis of chlorine residues in supported Pt and Pd catalysts with low metal loading. *Appl. Catal., A* **2003**, *247*, 283–294.
- (34) Paulis, M.; Peyrard, H.; Montes, M. Influence of chlorine on the activity and stability of Pt/Al<sub>2</sub>O<sub>3</sub> catalysts in the complete oxidation of toluene. *J. Catal.* **2001**, *199*, 30–40.
- (35) Gjervan, T.; Prestvik, R.; Tøtdal, B.; Lyman, C. E.; Holmen, A. The influence of the chlorine content on the bimetallic particle formation in Pt–Re/Al<sub>2</sub>O<sub>3</sub> studied by STEM/EDX, TPR, H<sub>2</sub> chemisorption and model reaction studies. *Catal. Today* **2001**, *65*, 163–169.
- (36) Balcells, D.; Raynaud, C.; Crabtree, R. H.; Eisenstein, O. The rebound mechanism in catalytic C–H oxidation by MnO(tpp)Cl from DFT studies: electronic nature of the active species. *Chem. Commun.* **2008**, *744–746*.
- (37) Xin, P.; Li, J.; Xiong, Y.; Wu, X.; Dong, J.; Chen, W.; Wang, Y.; Gu, L.; Luo, J.; Rong, H.; Chen, C.; Peng, Q.; Wang, D.; Li, Y. Revealing the active species for aerobic alcohol oxidation by using uniform supported palladium catalysts. *Angew. Chem., Int. Ed.* **2018**, *57*, 4642–4646.
- (38) Rohdenburg, M.; Martinović, P.; Ahlenhoff, K.; Koch, S.; Emmrich, D.; Gölzhäuser, A.; Swiderek, P. Cisplatin as a Potential Platinum Focused Electron Beam Induced Deposition Precursor: NH<sub>3</sub> Ligands Enhance the Electron-Induced Removal of Chlorine. *J. Phys. Chem. C* **2019**, *123*, 21774–21787.
- (39) Mäki-Arvela, P.; Murzin, D. Y. Effect of catalyst synthesis parameters on the metal particle size. *Appl. Catal., A* **2013**, *451*, 251–281.
- (40) Dhakshinamoorthy, J.; Prasad, A. K.; Dhara, S.; Pullithadathil, B. Anomalous Effects of Lattice Strain and Ti<sup>3+</sup> Interstitials on Room-Temperature Magnetic Ordering in Defect-Engineered Nano-TiO<sub>2</sub>. *J. Phys. Chem. C* **2018**, *122*, 27782–27794.
- (41) Feng, N.; Liu, F.; Huang, M.; Zheng, A.; Wang, Q.; Chen, T.; Cao, G.; Xu, J.; Fan, J.; Deng, F. Unravelling the efficient photocatalytic activity of boron-induced Ti<sup>3+</sup> species in the surface layer of TiO<sub>2</sub>. *Sci. Rep.* **2016**, *6*, 34765.
- (42) Ojha, R.; Boas, J. F.; Deacon, G. B.; Junk, P. C.; Bond, A. M. EPR spectroscopic characterization of a monomeric Pt<sup>III</sup> species produced via electrochemical oxidation of the anticancer compound trans-[Pt<sup>II</sup>{(p-HC<sub>6</sub>F<sub>4</sub>)NCH<sub>2</sub>CH<sub>2</sub>NEt<sub>2</sub>}Cl(py)]. *J. Inorg. Biochem.* **2016**, *162*, 194–200.
- (43) Frantz, S.; Fiedler, J.; Hartenbach, I.; Schleid, T.; Kaim, W. A complete series of tricarbonylhalidorhenium(I) complexes (abpy)Re-(CO)<sub>3</sub>(Hal), Hal=F, Cl, Br, I; abpy=2,2'-azobispyridine: Structures, spectroelectrochemistry and EPR of reduced forms. *J. Organomet. Chem.* **2004**, *689*, 3031–3039.
- (44) Voigt, A.; Abram, U.; Kirmse, R. EPR evidence of tetrahalogeno(triphenylmethylimido) rhenium (VI) complexes [Re{NC(C<sub>6</sub>H<sub>5</sub>)<sub>3</sub>}X<sub>4</sub>] (X= Cl, Br). *Inorg. Chem. Commun.* **1998**, *1*, 203–205.
- (45) Naldoni, A.; Altomare, M.; Zoppellaro, G.; Liu, N.; Kment, S.; Zboril, R.; Schmuki, P. Photocatalysis with reduced TiO<sub>2</sub>: From black TiO<sub>2</sub> to cocatalyst-free hydrogen production. *ACS Catal.* **2019**, *9*, 345–364.
- (46) Furukawa, S.; Shishido, T.; Teramura, K.; Tanaka, T. Photocatalytic oxidation of alcohols over TiO<sub>2</sub> covered with Nb<sub>2</sub>O<sub>5</sub>. *ACS Catal.* **2011**, *2*, 175–179.
- (47) Liu, N.; Schneider, C.; Freitag, D.; Hartmann, M.; Venkatesan, U.; Muller, J.; Spiecker, E.; Schmuki, P. Black TiO<sub>2</sub> nanotubes: cocatalyst-free open-circuit hydrogen generation. *Nano Lett.* **2014**, *14*, 3309–3313.
- (48) Konovalova, T. A.; Li, S.; Polyakov, N. E.; Focsan, A. L.; Dixon, D. A.; Kispert, L. D. Measuring Ti(III)-carotenoid radical interspin distances in TiMCM-41 by pulsed EPR relaxation enhancement method. *J. Phys. Chem. B* **2009**, *113*, 8704–8716.